Fifteenth International Conference on Solid State Lighting and LED-based Illumination Systems,
edited by Matthew H. Kane, Nikolaus Dietz, Ian T. Ferguson, Proc. of SPIE Vol. 9954,
99540R · © 2016 SPIE · CCC code: 0277-786X/16/$18 · doi: 10.1117/12.2237957

Effect of AlN buffer layers on the structural and optoelectronic properties of InN/AlN/Sapphire heterostructures grown by MEPA-MOCVD

M. K. Indika Senevirathna[1,a)], Daniel Seidlitz[1,2,3], Alireza Fali[1], Brendan Cross[1], Yohannes Abate[1,2], and Nikolaus Dietz[1,2]

[1]Department of Physics and Astronomy, Georgia State University, Atlanta GA 30303

[2]Center for Nano Optics, Georgia State University, Atlanta, GA 30303

[3]Institute of Solid State Physics, Technical University Berlin, Berlin, Germany

[a)] Electronic mail: mkindikas@phy-astr.gsu.edu

ABSTRACT

This contribution presents results on the structural and optoelectronic properties of InN layers grown on AlN/sapphire (0001) templates by Migration-Enhanced Plasma Assisted Metal Organic Chemical Vapor Deposition (MEPA-MOCVD). The AlN nucleation layer (NL) was varied to assess the physical properties of the InN layers. For ex-situ analysis of the deposited structures, Raman spectroscopy, Atomic Force Microscopy (AFM), and Fourier Transform Infrared (FTIR) reflectance spectroscopy have been utilized. The structural and optoelectronic properties are assessed by Raman-E_2 high FWHM values, surface roughness, free carrier concentrations, mobility of the free carriers, and high frequency dielectric function. This study focus on optimizing the AlN nucleation layer (e.g. temporal precursor exposure, nitrogen plasma exposure, plasma power and AlN buffer growth temperature) and its effect on the InN layer properties.

Keywords: InN, AlN, migration-enhanced plasma-assisted MOCVD, FTIR reflectance, Raman, High frequency dielectric constant, AFM, Free carrier concentration, Mobility

I. INTRODUCTION

Due to the narrow direct band gap of Indium nitride (InN), its small effective mass, high electron mobility and high drift velocity, indium-rich group III-nitride alloys are of high interest for photovoltaic-, electronic-, and optoelectronic device applications.[1-4] Furthermore, InN containing heterostructures might be utilized the performance of electronic devices such as sensors and terahertz emitters.[5, 6] However, the growth of high quality InN is a challenge, due to the high partial pressure of nitrogen at optimum growth temperatures above the growth surface. Ammonia, the main nitrogen source used in the traditional CVD/MOCVD growth of InN, decomposes at a temperature above 900 °C, which is greater than the decomposition temperature of InN. Additionally, the growth of multinary indium-rich group III-nitrides, is further challenged due to the differences in the partial pressures of the group III-N binaries, requiring the adjustment of the growth processing parameters for each target composition. In order to reduce the growth temperature gaps between the binaries and to control the growth surface chemistry, several advanced growth techniques are presently explored. For example, super-atmospheric pressure chemical vapor deposition (denoted as HPCVD),[7-10] atomic layer deposition (ALD), plasma-assisted ALD,[11] and migration-enhanced, plasma-assisted metalorganic chemical vapor deposition (MEPA-MOCVD),[12-16] are explored to assess the control of the vastly different partial pressures and surface chemistries by thermodynamic and/or kinetic means. However, at present, the layers grown by the various growth methods exhibit variations in their measured physical properties (e.g. free carrier concentrations, optical band gap, structural quality, etc.), leading to widely speculative assumptions on the fundamental properties of InN and indium-rich alloys. In this

contribution, we evaluate the layer properties of group III-N alloys grown by MEPA-MOCVD using plasma activated nitrogen species/ fragments as nitrogen precursors that are directed to the growth surface in the afterglow regime. The MEPA-MOCVD reactor system is equipped with a load lock system, metalorganic precursors (MO's) showerhead injection system, and a MEAglow oxygen-free hollow cathode N_2 plasma source to generate energy-controlled active nitrogen species and the afterglow regime above the growth surface. The reactor pressure can be operated in the range of 1 mbar -10 mbar. The MO and plasma-activated nitrogen precursor species can be supplied temporal and spatially separated, which allows controlling the surface diffusion processes of adatoms at the growth surface. The plasma-activated nitrogen species are formed at much lower temperatures compared to conventionally used ammonia as the nitrogen precursor. At present, the vast growth parameter space in MEPA-MOCVD is hardly explored. In this study, we focus only on the crystalline quality of the InN epilayer grown on various AlN interlayers deposited at growth temperatures between 550 and 780 °C. As widely reported in the literature,[17, 18] the AlN interlayer between sapphire (c-Al_2O_3) and a group III-nitride epilayer plays a critical role in the transition from a metal-oxygen surface chemistry to a metal-nitrogen chemistry, reducing dislocation and defect densities in the subsequent group III-N overgrowth process. However, lattice mismatch induced strain has to be still dealt with in the InN/AlN overgrowth process.

II. EXPERIMENTAL

Group III-N heterostructures were deposited on sapphire (0001) substrate using a customized MEPA-MOCVD reactor, which details are provided elsewhere.[12, 15, 19] A MEAglow plasma source is used to provide controlled nitrogen fragments in an afterglow regime towards the growth surface. As schematically illustrated in Fig. 1, a spatial and temporal controlled injection of MO's and plasma-activated nitrogen precursor injection scheme is used in this study. The deposition of InN and AlN epilayers were examined by varying, growth temperature, plasma power, and plasma exposure time. In order to study the influence of the AlN interlayer between the sapphire and the subsequent InN layer, the growth conditions for the InN layer were taken from a previous study[19] and kept constant with a reactor pressure of 3.3 Torr, a growth temperature of 775 °C, a pulsed plasma power of 400 W (14 s), followed by a TMI (Trimethylindium) pulse of 1 sec (9.6 µmol/min). The deposition conditions for the AlN buffer layers were varied as described in the result section.

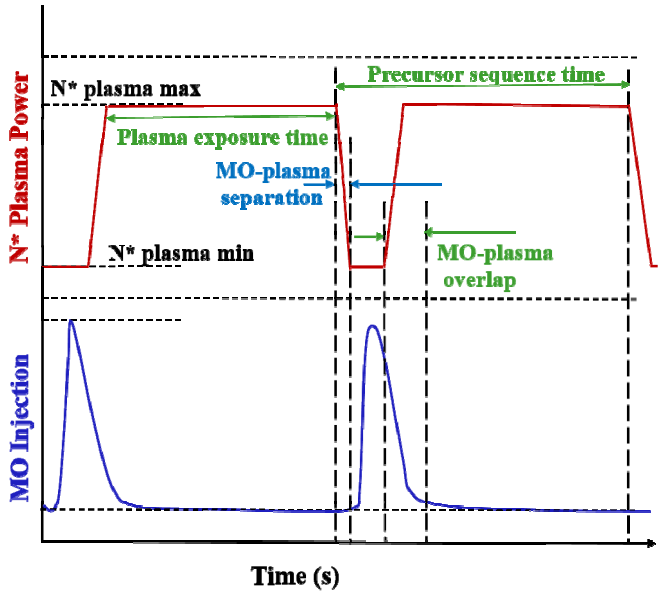

Figure 1 Schematic illustration for temporal separated MO and N*-plasma precursor injection.

The InN layers grown on top of the AlN buffer layers were characterized by AFM, FTIR reflection- and Raman spectroscopy. In order to analyze the local crystalline order, the Raman spectra of the samples were taken at room temperature in z (xx)-z back scattering geometry with excitation energy of 2.33 eV. Here, a customized Raman set up was utilized, based on a single 2m-monochromator and a liquid N_2-cooled multichannel CCD (Charge-Couple Detector). The surface morphology of the layers was analyzed by AFM.

The IR reflection measurements were performed at room temperature, at near normal incidence (~8°) configuration using a Perkin-Elmer 2000 FTIR spectrophotometer. A MCT (HgCdTe) detector and KBr beam splitter were used to cover the spectral range of 450 - 6500 cm^{-1}.

III. RESULTS AND DISCUSSION

Initial growth of AlN buffer layers were carried out at a growth temperature of 775°C, a reactor pressure of 3.3 Torr, and a plasma power of 400 W, followed by a subsequent deposition of an InN epilayer. In the first series, the precursor trimethylaluminum (TMA) and plasma activated nitrogen (PAN) were introduced temporally spaced with a 1 sec TMA injection following a PAN exposure time that was varied from 4 s to 12 s.

The E_2(high) and A_1(LO) phonon modes for the wurtzite structure of the AlN, should be observed around 657 cm^{-1} and 890 cm^{-1}.[20] In our Raman spectra, these two modes were very weak, which might be due to the very low thickness of the AlN layer or the limited AlN crystallinity. Surface morphology studies of the layers were carried out by AFM. Figure 2 shows the AFM topography and corresponding island height-vs-position plots for sapphire (a) and the AlN layers grown with 4 s (b), 8 s (c), and 12 s (d) PAN exposure time, respectively. The corresponding surface RMS roughness in a 0.5×0.5 μm^2 area are 0.245 nm, 2.4 nm, 2.16 nm and 1.36 nm, respectively. The RMS surface roughness is calculated using the following equation:

$$R_q = \sqrt{\frac{1}{N}\sum_{i}^{N}\left(Z_i - Z_{ave}\right)^2}; \qquad \text{where,} \quad Z_{ave} = \sum_{i}^{N} Z_i / N \tag{1}$$

Here, Z_i, N, and Z_m are the height at the i [th] row or column of the surface scan, number of rows and columns of the scanned area, and average height, respectively.

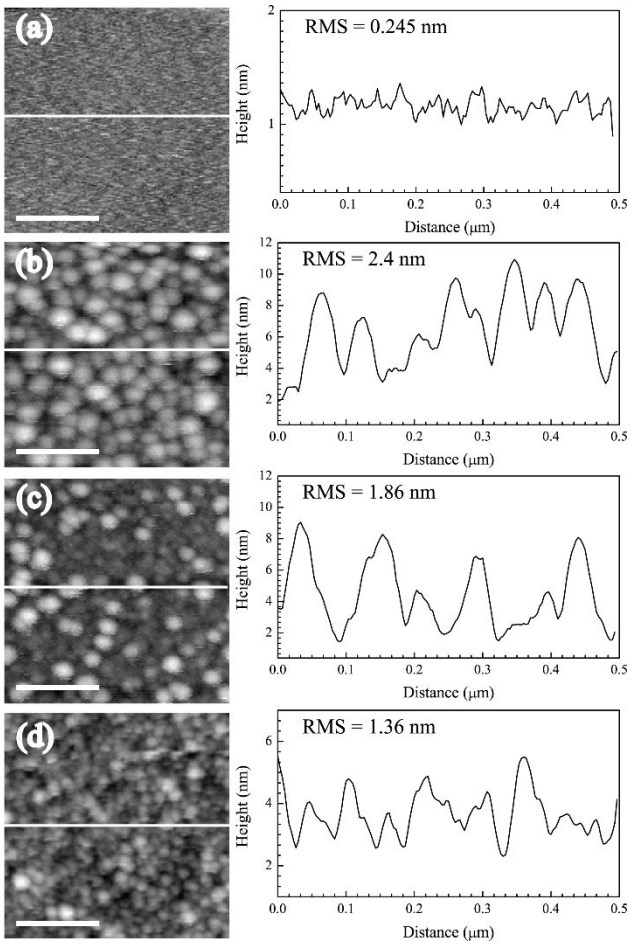

Figure 2 2D-AFM surface topography (scale bar = 200 nm) of sapphire (a) and AlN buffer layers grown with 4 s (b), 8 s (c), and 12 s (d) plasma exposure per pulse. On the right are the corresponding AFM height profiles. The scan area is 0.5×0.5 μm^2.

The results show that a longer plasma pulse exposure time (12 s) leads to a smoother layer surface, with a smaller grain size, and a higher grain density compared to AlN nucleation layers grown at 4 s and 8 s. Increasing the plasma exposure time, increases the growth surface nitridation which can result in higher nuclei density. The efficiency of the nitridation procedure depends on the concentration of active nitrogen species at the growth surface and the amount of active nitrogen generated via the hollow cathode source (e.g. plasma power and N_2 flow).

In order to study the influence of the plasma power on plasma activated nitrogen species on the growth chemistry and the related surface morphology, a set of AlN samples were grown with a 12 s PAN exposure time and a variation of the plasma power from 300 W to 500 W. The AFM topography and corresponding height profiles of the AlN surfaces at 300 W, 400 W, and 500 W are depicted in the Fig. 3.

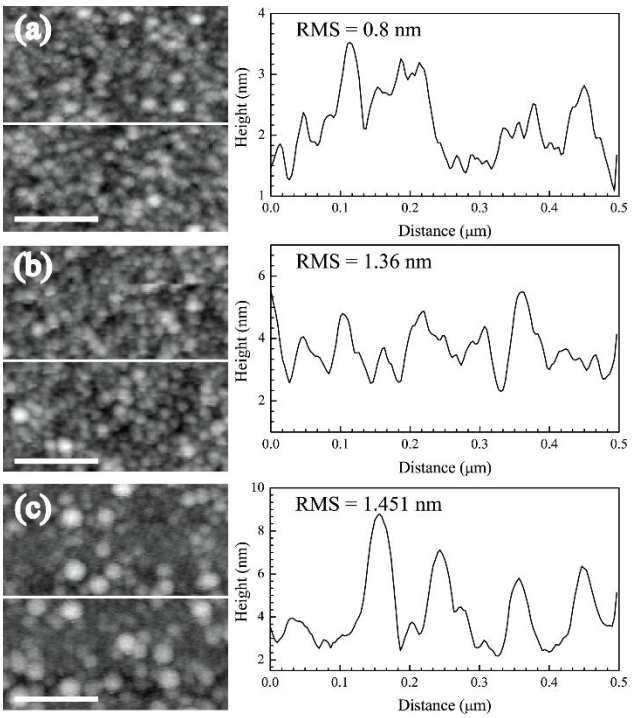

Figure 3 2D-AFM surface topography (scale bar = 200 nm) within a 0.5×0.5 μm^2 scan area and corresponding profile of change in the height along distance for AlN-NL grown at (a) 300 W, (b) 400 W, and (c) 500 W plasma power. The RMS surface roughness values are 0.8 nm, 1.36 nm, and 1.451 nm, respectively.

The results show that the surface roughness increases with plasma power, which suggests that the energies of the PAN species are too high. An increase of hollow cathode plasma power changes not only the kinetic energies of the activated nitrogen species, but also the type of nitrogen species in the afterglow regime above the growth surface. Consequently, we can expect damage to the growth surface at higher plasma power, which may lead to a higher surface roughness. On the other hand, AFM topography shows the highest grain size and lowest nuclei density for the sample grown at 500 W plasma power. Since a higher grain size of AlN buffer improves the crystalline quality of a subsequent overgrown GaN layers[21], the 500W plasma power was used in the growth of AlN buffer layer in further studies.

As discussed in the literature,[21] the quality of an AlN layer may improve upon thermal annealing. Thus, we annealed the AlN-NLs grown at 775 °C for 60 minutes. The injection of plasma and MO were continuous during the growth. The annealing temperature was varied from 800 °C to 875 °C at 3 Torr N_2 pressure. Figure 4 depicts the AFM 2D-3D topography for as-grown AlN layer, and AlN layers annealed at various annealing temperatures with 800 °C, 825 °C 850 °C, 875 °C, respectively.

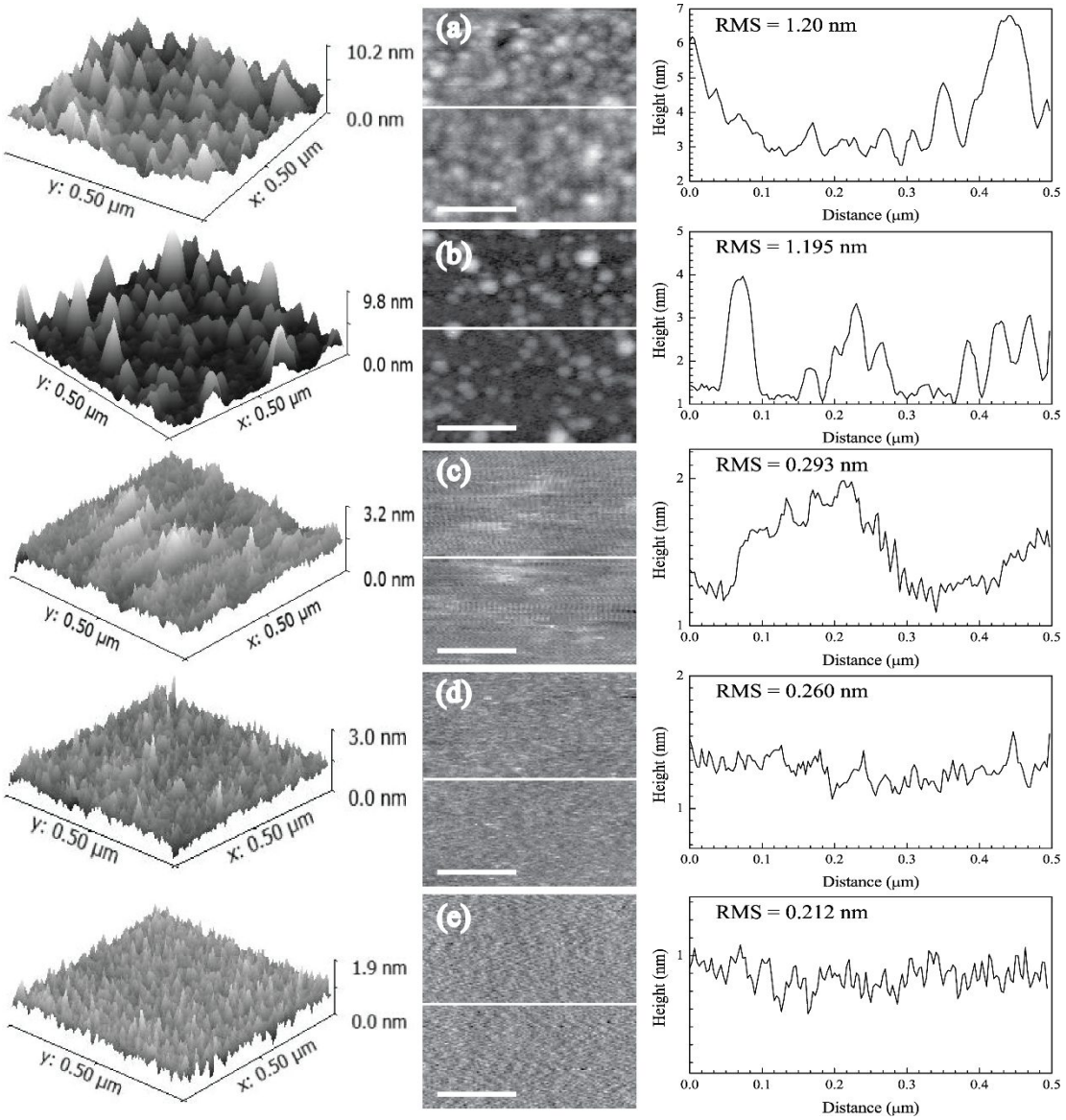

Figure 4 2D-AFM surface topography (scale bar = 200 nm) of (a) as- grown AlN-NL and annealing temperature of AlN -NL layers at (b) 800 °C, (c) 825 °C, (d) 850 °C and (e) 875 °C. On the left and right are the corresponding AFM 3D topography and the height profiles. The scan area is 0.5×0.5 μm^2.

The RMS surface roughness values versus annealing temperature are shown in Fig. 5.

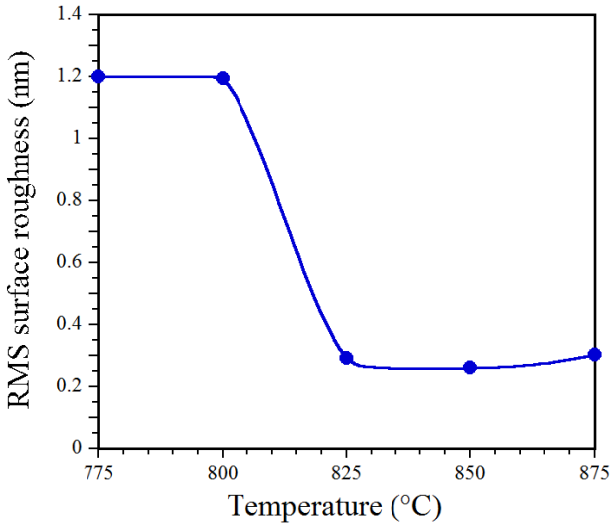

Figure 5 RMS surface roughness vs annealing temperature.

These results show that the RMS surface roughness of the AlN layers improves with the annealing temperature of the deposited AlN layers. With increasing the annealing temperature, the RMS surface roughness values reduces from 1.2 nm to 0.212 nm indicating an atomically flat surface. To evaluate the influence of the annealed AlN layer on the crystalline quality, the Raman spectra were taken for the post-annealing AlN layers. As shown in Fig. 6 with increasing annealing temperature, the Raman $A_1(LO)$ phonon mode appears at 890 cm^{-1} for the AlN buffer layer annealed at 850 °C, indicating an improvement of the crystalline quality of the AlN layer.

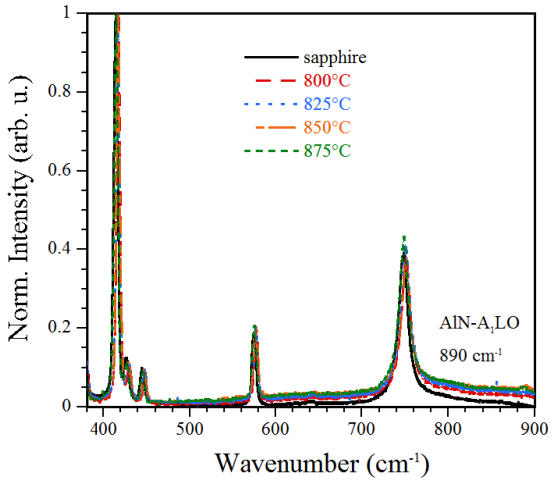

Figure 6 Raman spectra for the AlN buffer grown on sapphire by varying post-annealing temperature, (long-dashed)) 800 °C, (dotted) 825 °C, (dashed-long dashed) 850 °C, (dashed) 875 °C, and (solid) sapphire.

In the following step, we investigated the crystalline quality and surface morphology of InN layers as a function of the AlN/sapphire template. First, an InN sample was grown on sapphire. The second InN layer was grown on an AlN template which was not annealed. The third InN layer was grown on AlN layer which was subsequently annealed at 850

°C for 60 minutes. For all InN films, a mirror-like surface was observed. Figures 7, 8, and 9 depict (a) 2D-AFM and (b) 3D-AFM topographies for the various InN layers deposited.

The three samples investigated show that the InN islands density decreases if an AlN buffer is added and the AlN layer is annealed. At the same time, the lateral size of the islands increases. These results indicate that an annealed AlN buffer layer between sapphire and InN layers leads to an improved surface morphology of subsequent InN layer, with a RMS surface roughness value of 2.02 nm for the AlN layer annealed at 850 °C/sapphire.

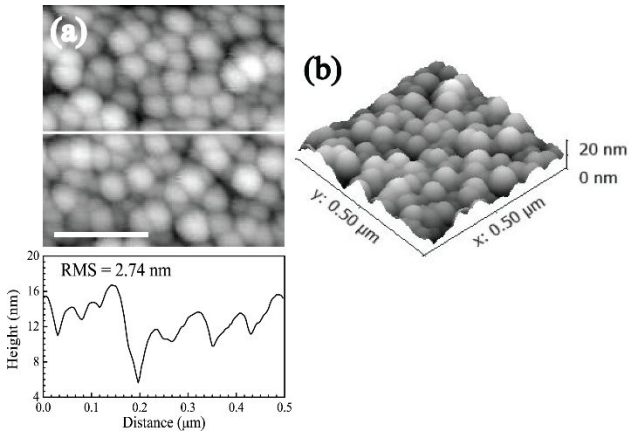

Figure 7 (a) 2D-AFM surface image (scale bar = 200 nm) with the corresponding profile of change in the height along position, (b) 3D-AFM surface topography for the InN/sapphire. The scan area is $0.5\times0.5\mu m^2$.

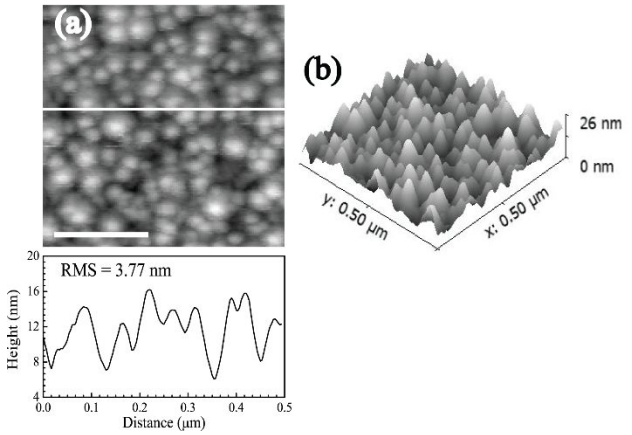

Figure 8 2D-AFM surface image (scale bar = 200 nm) with the profile of change in the height along distance, and (b) 3D-AFM surface topography for the InN/AlN/sapphire. The scan area is $0.5\times0.5\ \mu m^2$.

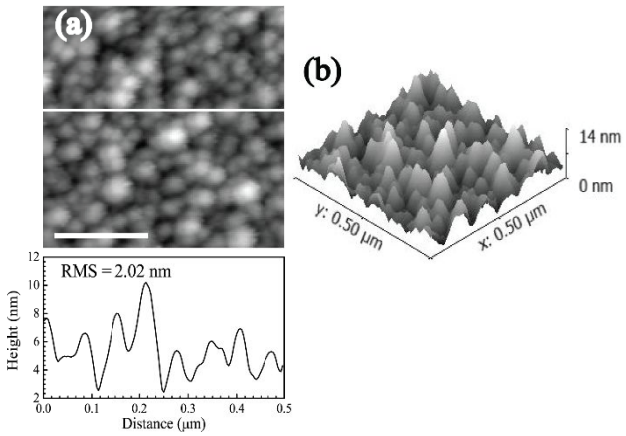

Figure 9 (a) 2D-AFM surface image (scale bar = 200 nm) with the profile of change in the height along distance, and (b) 3D-AFM surface topography for the InN/AlN-annealed at 850 °C/sapphire. The scan area is 0.5×0.5 μm^2.

For the layers investigated by Raman spectroscopy, the InN epilayer grown directly on sapphire exhibit a pronounced Raman E_2(high) mode, indicating a good local crystalline ordering of the InN epilayer. As depicted in Fig. 10, the Raman spectrum for the InN layer grown on top of AlN buffer layer (dashed line) shows an improved E_2(high) mode, which is further improved if the AlN layer is annealed (dashed line). The E_2(high) and A_1(LO) phonon modes are observed at ~ 488 cm^{-1} and ~586 cm^{-1} respectively.[22] In addition to these two modes, the sapphire phonon modes at 749 cm^{-1} and 575 cm^{-1} are observed. These modes diminish for thicker InN epilayers. The broadening and strength of the A_1(LO) mode in the layers is attributed to the high free carrier concentration in the films.[23], while the broadened E_2(high) mode relates to the local structural disorder (point and extended defects) in the InN layers. The FWHM values of the E_2(high) mode of the three InN layers are 14.3 cm^{-1}, 12.2 cm^{-1}, and 11.5 cm^{-1}, respectively. We also observe a decrease of the Raman background scattering for the InN layers grown with AlN layers, which is related to structural defects and/or metallic inclusions. Further experiments are needed to improve the local crystallinity of the InN layers.

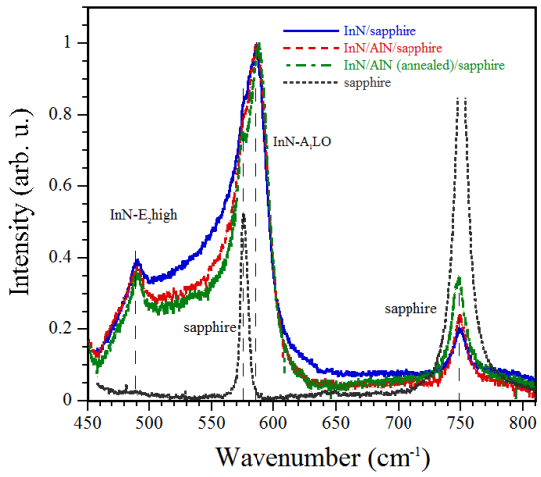

Figure 10 The Raman spectra for the InN/sapphire (solid), InN/AlN/sapphire (dashed), and InN grown on AlN annealed at 850°C /sapphire (dotted-dashed), and sapphire (dotted).

FTIR reflectance measurements were carried out to extract the free carrier concentration, mobility of the carriers, and high frequency dielectric function of the InN layers. Figure 11 summarizes the experimental FTIR reflectance spectra for InN/sapphire (dotted line), InN/AlN/sapphire (solid line), and InN grown on post-annealed (at 850 °C) AlN buffer/sapphire (dashed line).

To extract the layer properties, a multilayer stack model and a fit program are used. The dielectric function in the IR region is approximated using the Lorentz-Drude model[24] and effective high frequency dielectric function ε_∞, accounting for the lattice (phonon) contributions, free carrier contributions, and the contribution due to the inter-band transitions, respectively (see Eq. (2)).

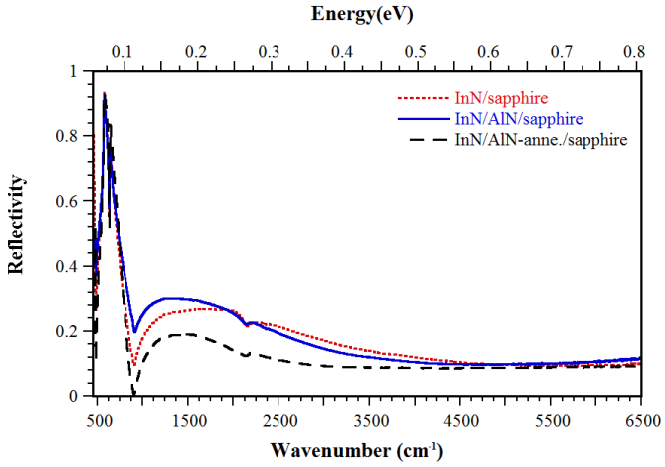

Figure 11 The experimental reflectance spectra for InN/sapphire (dotted line), InN/AlN/sapphire (solid line), and InN/AlN annealed at 850 °C/sapphire (dashed line).

$$\varepsilon(\omega) = \varepsilon_\infty \cdot \left(1 + \frac{\omega_{LO}^2 - \omega_{TO}^2}{\omega_{TO}^2 - \omega^2 - i \cdot \omega \cdot \gamma_p} - \frac{\omega_p^2}{\omega^2 + i \cdot \omega \cdot \tau} \right) \tag{2}$$

Here, ω_{TO}, ω_{LO}, and γ_p are the TO, LO phonon frequencies and broadening parameter of the phonons. ω_p and τ are the plasma frequency and the damping constant of plasma. ε_∞ is the high frequency dielectric constant. The free carrier concentration and mobility of the carriers were calculated by using following Eq. (3) and Eq. (4).

$$n_c = \frac{{\omega_p}^2 m_{eff} \varepsilon_\infty \varepsilon_0}{q^2} \tag{3}$$

$$\mu = \frac{q}{m_{eff} \tau} \tag{4}$$

Here, n_c, q, m_{eff}, and μ are the free carrier concentration, the electron charge, the effective mass of the carriers and the free carrier mobility, respectively. Each layer in the multilayer stack is parameterized with layer thickness, effective dielectric function, and interfacial imperfection parameter, which allows establishing a model reflectance spectrum, which is fitted to the experimental spectrum.[25] A nonlinear fitting algorithm was used to determine the best fit parameter for the layers.[24]

The experimental and calculated FTIR reflectance spectra for InN/AlN/sapphire are depicted in Fig. 12. The inset shows the modeled three-layer stack structure used to determine the parameter of the InN layer. The AlN interlayer

was not resolvable in the model configuration. The other two samples were modeled in the manner. The extracted layer thickness, high frequency dielectric constant, free carrier concentration and the mobility of the free carries for each InN layers are summarized in Table I. The free carrier concentration was confirmed by the Hall measurements.

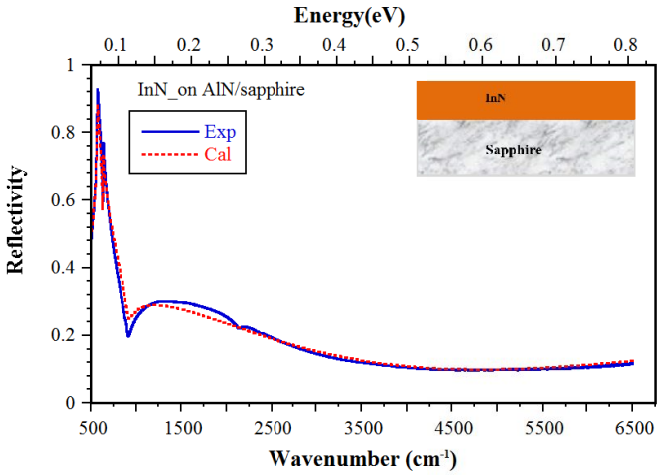

Figure 12 Experimental (solid line) and best fit (dashed line) IR reflectance spectra for InN/AlN/sapphire. Inset shows the layer structure used for best fit.

Table I The best fit InN layer parameters, thickness (d), high frequency dielectric constant (ε_∞), free carrier concentration, and mobility obtained from the FTIR reflectance simulation.

Sample	Thickness (nm)	ε_∞	Free carrier conc. (cm^{-3})	Mobility ($cm^2V^{-1}s^{-1}$)
InN/sapphire	64	5.78	9.5×10^{19}	57
InN/AlN/sapphire	80	5.96	7.6×10^{19}	72
InN/AlN(annealed)/sapphire	54	5.81	5.6×10^{19}	85

These results show an improvement in free carrier concentration and mobility of the free carriers for InN films grown on AlN buffer and annealed at 850 °C. As discussed in the literature,[26-28] the mobility and electron concentration depends on the InN layer thickness and has to be greater than 0.5 µm in order to achieve a mobility above 1000 $cm^2V^{-1}s^{-1}$ and an electron concentration below 10^{18} cm^{-3}. As indicated in Table I, there is no significant influence of high frequency dielectric constant of the layers grown with without AlN buffer layer, which indicates that the optical density of the layers remains. Literature data report large variations for high frequency dielectric constant ε_∞, varying from 10.8 to 5.03[29, 30], with a ε_∞ value reported as 8.4 for InN wurtzite structure[31-34]. Later studies used this value to calculate the free carrier concentration and mobility of InN layers[35-39]. Bernardini et al.[40, 41] calculated the high frequency constant InN as 8.49 using geometric quantum phase polarization theory and density-functional theory. Inushima et al.[42] obtained a ε_∞ value of 5.8 using Kramers–Konig analysis of reflectivity data for InN layer grown on sapphire by ALE (atomic layer epitaxy). Qian et al.[43] used a value of $\varepsilon_\infty = 5.8$ to obtain the mobility and free carrier concentration of InN layers grown on GaAs and the sapphire substrate using RF magnetron sputtering. Different values of ε_∞ = 5.03, 7.054, 7.27, and 8.1 have been obtained from different theoretical models[30] assuming InN wurtzite structure. Kasic et al.[44] utilized infrared spectroscopic ellipsometry data (IR-SE) data to determine a ε_∞ value of 6.7. Later studies [23, 45-55] of InN based on IR-SE, IR reflectivity data or Raman data used this value to calculate the free carrier concentration, mobility, effective mass, etc.. Ishitani et al.[56] determined a ε_∞ of 8.3 by IR reflectivity data measured at 296 K and 5 K temperature. In 2006, Fukuik et al.[57] obtained ε_∞ as 8.5 from the IR reflectivity data analysis for the InN grown on sapphire by OMVPE.

Schley et al.[58] obtained ε_∞ as 7.84 and 7.76 by IR-SE data analysis for the In-face and N-face InN layers, grown by plasma-induced molecular beam epitaxy. In the previous studies[10], we obtained a ε_∞ value of 5.78 for InN grown on GaN/sapphire by HPCVD. This value is closer to the value reported by Inushima et al.[42]. In our other study,[24] we obtained ε_∞ values varying between 5.29 and 7.69 for different InN layers grown at different reactor pressure by HPCVD. Model simulations of IR-SE data by Himmerlich et al.[59] suggest that ε_∞ is strongly influenced by carbon doping concentration and may vary from 7.64 for undoped InN layer (7.4×10^{17} cm^{-3}) to 7.28 for doped layer (3.5×10^{18} cm^{-3}) grown on GaN/sapphire by MBE. Zang et al.[29] determined ε_∞ for InN grown on sapphire by PR-MOVPE (pressurized-reactor metalorganic vapor phase epitaxy) at different growth temperature. The ε_∞ values obtained from IR reflectance analysis varied from 10.8, 6.0, and 6.3 for 500 °C, 600 °C, and 700 °C, respectively.

All these results indicate the large variation of the high frequency dielectric constant ε_∞ for InN layers grown with various growth techniques. This might be related to extended defects, voids in the bulk material, a shift in the effective band structure, or the calculation methods used to determine the dielectric constant. These uncertainties in ε_∞ makes it difficult to compare the obtained ε_∞ values for our InN layers with reported values. However, the obtained ε_∞ high frequency dielectric constants of InN layers from this study are close the value of 5.8 obtained by Inushima et al.[42].

IV. CONCLUSION

We presented first results on the structural and optoelectronic properties of InN layers grown on AlN buffer layer/sapphire (0001) by Migration-Enhance Plasma Assisted Metal Organic Chemical Vapor Deposition (MEPA-MOCVD). The results indicate that an AlN buffer layer annealed at 850 °C, between the InN layer and sapphire improves the structural quality and optoelectronic properties of overgrown InN layers. Further improvements on the AlN buffer layer quality and InN growth processing parameters are needed to further improve the structural quality of the InN epilayers and their optoelectronic properties.

V. ACKNOWLEDGEMENT

This work is financially supported by Air Force Office of Scientific Research (AFOSR) under award # FA9550-10-1-0097, YA and AF acknowledge support for this work from the Air Force Office of Scientific Research (AFOSR) grant number FA9559-16-1-0172 and GSU-PRE. Authors also acknowledge Dr. A.G.U. Perera for providing his laboratory facilities for the FTIR reflectance measurements.

VI. REFERENCES

[1] Matsuoka, T., Okamoto, H., Nakao, M., Harima, H. and Kurimoto, E., "Optical bandgap energy of wurtzite InN," Applied Physics Letters **81** (7), 1246-1248 (2002).

[2] Wu, J., Walukiewicz, W., Yu, K. M., III, J. W. A., Haller, E. E., Lu, H., Schaff, W. J., Saito, Y. and Nanishi, Y., "Unusual properties of the fundamental band gap of InN," Applied Physics Letters **80** (21), 3967-3969 (2002).

[3] Bhuiyan, A. G., Hashimoto, A. and Yamamoto, A., "Indium nitride (InN): A review on growth, characterization, and properties," Journal of Applied Physics **94** (5), 2779-2808 (2003).

[4] Wu, J., Walukiewicz, W., Yu, K. M., Shan, W., III, J. W. A., Haller, E. E., Lu, H., Schaff, W. J., Metzger, W. K. and Kurtz, S., "Superior radiation resistance of In[sub 1 - x]Ga[sub x]N alloys: Full-solar-spectrum photovoltaic material system," Journal of Applied Physics **94** (10), 6477-6482 (2003).

[5] Lu, H., Schaff, W. J. and Eastman, L. F., "Surface chemical modification of InN for sensor applications," Journal of Applied Physics **96** (6), 3577-3579 (2004).

[6] Starikov, E., Shiktorov, P., Gružinskis, V., Reggiani, L., Varani, L., Vaissière, J. C. and Zhao, J. H., "Monte Carlo calculations of THz generation in wide gap semiconductors," Physica B: Condensed Matter **314** (1–4), 171-175 (2002).

[7] Woods, V., Born, H., Strassburg, M. and Dietz, N., "Real time optical characterization of gas flow dynamics in high-pressure chemical vapor deposition," Journal of Vacuum Science & Technology A **22** (4), 1596-1599 (2004).

[8] Dietz, N., Alevli, M., Woods, V., Strassburg, M., Kang, H. and Ferguson, I. T., "The characterization of InN growth under high-pressure CVD conditions," physica status solidi (b) **242** (15), 2985-2994 (2005).
[9] Woods, V. and Dietz, N., "InN growth by high-pressures chemical vapor deposition: Real-time optical growth characterization," Materials Science and Engineering: B **127** (2–3), 239-250 (2006).
[10] Buegler, M., Gamage, S., Atalay, R., Wang, J., Senevirathna, M. K. I., Kirste, R., Xu, T., Jamil, M., Ferguson, I., Tweedie, J., Collazo, R., Hoffmann, A., Sitar, Z. and Dietz, N., "Growth temperature and growth rate dependency on reactor pressure for InN epilayers grown by HPCVD," physica status solidi (c) **8** (7-8), 2059-2062 (2011).
[11] Haider, A., Kizir, S., Ozgit-Akgun, C., Goldenberg, E., Leghari, S. A., Okyay, A. K. and Biyikli, N., "Low-temperature grown wurtzite $In_xGa_{1-x}N$ thin films via hollow cathode plasma-assisted atomic layer deposition," Journal of Materials Chemistry C **3** (37), 9620-9630 (2015).
[12] Butcher, K. S. A., Alexandrov, D., Terziyska, P., Georgiev, V. and Georgieva, D., "Initial experiments in the migration enhanced afterglow growth of gallium and indium nitride," physica status solidi (c) **9** (3-4), 1070-1073 (2012).
[13] Binsted, P. W., Butcher, K. S. A., Alexandrov, D., Terziyska, P., Georgieva, D., Gergova, R. and Georgiev, V., "InN on GaN Heterostructure Growth by Migration Enhanced Epitaxial Afterglow (MEAglow)," MRS Online Proceedings Library Archive **1396** (2012).
[14] Butcher, K. S. A., Alexandrov, D., Terziyska, P., Georgiev, V., Georgieva, D. and Binsted, P. W., "InN grown by migration enhanced afterglow (MEAglow)," physica status solidi (a) **209** (1), 41-44 (2012).
[15] Butcher, K. S. A., Kemp, B. W., Hristov, I. B., Terziyska, P., Binsted, P. W. and Alexandrov, D., "Gallium Nitride Film Growth Using a Plasma Based Migration Enhanced Afterglow Chemical Vapor Deposition System," Japanese Journal of Applied Physics **51** (1S), 01AF02 (2012).
[16] Togtema, G., Georgiev, V., Georgieva, D., Gergova, R., Butcher, K. S. A. and Alexandrov, D., "GaN–InGaN LED efficiency reduction from parasitic electron currents in p-GaN," Solid-State Electronics **103**, 44-48 (2015).
[17] Zhao, D. G., Jiang, D. S., Wu, L. L., Le, L. C., Li, L., Chen, P., Liu, Z. S., Zhu, J. J., Wang, H., Zhang, S. M. and Yang, H., "Effect of dual buffer layer structure on the epitaxial growth of AlN on sapphire," Journal of Alloys and Compounds **544**, 94-98 (2012).
[18] Lu, H., Schaff, W. J., Hwang, J., Wu, H., Koley, G. and Eastman, L. F., "Effect of an AlN buffer layer on the epitaxial growth of InN by molecular-beam epitaxy," Applied Physics Letters **79** (10), 1489-1491 (2001).
[19] Seidlitz, D., Senevirathna, M. K. I., Abate, Y., Hoffmann, A. and Dietz, N., " Optoelectronic and structural properties of InGaN grown by Migration-Enhanced, Plasma-Assisted MOCVD," Fourteenth International Conference on Solid State Lighting and LED-based Illumination Systems, San Diego, CA, Proc. SPIE 9571, paper 95710P (2015).
[20] Davydov, V. Y., Kitaev, Y. E., Goncharuk, I. N., Smirnov, A. N., Graul, J., Semchinova, O., Uffmann, D., Smirnov, M. B., Mirgorodsky, A. P. and Evarestov, R. A., "Phonon dispersion and Raman scattering in hexagonal GaN and AlN," Physical Review B **58** (19), 12899-12907 (1998).
[21] Zhao, D. G., Zhu, J. J., Liu, Z. S., Zhang, S. M., Yang, H. and Jiang, D. S., "Surface morphology of AlN buffer layer and its effect on GaN growthby metalorganic chemical vapor deposition," Applied Physics Letters **85** (9), 1499-1501 (2004).
[22] Harima, H., "Properties of GaN and related compounds studied by means of Raman scattering," Journal of Physics: Condensed Matter **14** (38), R967 (2002).
[23] Thakur, J. S., Haddad, D., Naik, V. M., Naik, R., Auner, G. W., Lu, H. and Schaff, W. J., "${A}_{1}(\mathrm{LO})$ phonon structure in degenerate InN semiconductor films," Physical Review B **71** (11), 115203 (2005).
[24] Indika Senevirathna, M. K., Gamage, S., Atalay, R., Acharya, A. R., Unil Perera, A. G., Dietz, N., Buegler, M., Hoffmann, A., Su, L., Melton, A. and Ferguson, I., "Effect of reactor pressure on the electrical and structural properties of InN epilayers grown by high-pressure chemical vapor deposition," Journal of Vacuum Science & Technology A **30** (3), 031511 (2012).
[25] Dietz, N., "Real-time optical characterization of thin film growth," Materials Science and Engineering: B **87** (1), 1-22 (2001).
[26] Xinqiang, W., Shitao, L., Nan, M., Li, F., Guang, C., Fujun, X., Ning, T., Sen, H., Kevin, J. C., Shengqiang, Z. and Bo, S., "High-Electron-Mobility InN Layers Grown by Boundary-Temperature-Controlled Epitaxy," Applied Physics Express **5** (1), 015502 (2012).

[27] Junichi, S., Tsutomu, A., Tatsuya, F., Elison, M., Tomás, P. and Yasushi, N., "Thickness Dependence of Structural and Electrical Properties of Thin InN Grown by Radio-Frequency Plasma-Assisted Molecular Beam Epitaxy," Japanese Journal of Applied Physics **52** (8S), 08JD06 (2013).
[28] Ruffenach, S., Moret, M., Briot, O. and Gil, B., "Recent advances in the MOVPE growth of indium nitride," physica status solidi (a) **207** (1), 9-18 (2010).
[29] Zhang, Y., Kimura, T., Prasertusk, K., Iwabuchi, T., Kumar, S., Liu, Y., Katayama, R. and Matsuoka, T., "Optical properties of InN films grown by pressurized-reactor metalorganic vapor phase epitaxy," Thin Solid Films **536**, 152-155 (2013).
[30] in *Group IV Elements, IV-IV and III-V Compounds. Part a - Lattice Properties*, edited by O. Madelung, U. Rössler and M. Schulz (Springer Berlin Heidelberg, Berlin, Heidelberg, 2001), pp. 1-3.
[31] Morkoç, H., Strite, S., Gao, G. B., Lin, M. E., Sverdlov, B. and Burns, M., "Large-band-gap SiC, III-V nitride, and II-VI ZnSe-based semiconductor device technologies," Journal of Applied Physics **76** (3), 1363-1398 (1994).
[32] Mohammad, S. N. and Morkoç, H., "Progress and prospects of group-III nitride semiconductors," Progress in Quantum Electronics **20** (5–6), 361-525 (1996).
[33] O'Leary, S. K., Foutz, B. E., Shur, M. S., Bhapkar, U. V. and Eastman, L. F., "Electron transport in wurtzite indium nitride," Journal of Applied Physics **83** (2), 826-829 (1998).
[34] Yu, S., Kim, K. W., Bergman, L., Dutta, M., Stroscio, M. A. and Zavada, J. M., "Long-wavelength optical phonons in ternary nitride-based crystals," Physical Review B **58** (23), 15283-15287 (1998).
[35] Tansley, T. L. and Egan, R. J., "Point-defect energies in the nitrides of aluminum, gallium, and indium," Physical Review B **45** (19), 10942-10950 (1992).
[36] Chin, V. W. L., Tansley, T. L. and Osotchan, T., "Electron mobilities in gallium, indium, and aluminum nitrides," Journal of Applied Physics **75** (11), 7365-7372 (1994).
[37] Dyck, J. S., Kim, K., Limpijumnong, S., Lambrecht, W. R. L., Kash, K. and Angus, J. C., "Identification of Raman-active phonon modes in oriented platelets of InN and polycrystalline InN," Solid State Communications **114** (7), 355-360 (2000).
[38] Qian, Z. G., Shen, W. Z., Ogawa, H. and Guo, Q. X., "Infrared reflection characteristics in InN thin films grown by magnetron sputtering for the application of plasma filters," Journal of Applied Physics **92** (7), 3683-3687 (2002).
[39] Davydov, V. Y., Emtsev, V. V., Goncharuk, I. N., Smirnov, A. N., Petrikov, V. D., Mamutin, V. V., Vekshin, V. A., Ivanov, S. V., Smirnov, M. B. and Inushima, T., "Experimental and theoretical studies of phonons in hexagonal InN," Applied Physics Letters **75** (21), 3297-3299 (1999).
[40] Bernardini, F., Fiorentini, V. and Vanderbilt, D., "Polarization-Based Calculation of the Dielectric Tensor of Polar Crystals," Physical Review Letters **79** (20), 3958-3961 (1997).
[41] Bernardini, F. and Fiorentini, V., "Electronic dielectric constants of insulators calculated by the polarization method," Physical Review B **58** (23), 15292-15295 (1998).
[42] Inushima, T., Shiraishi, T. and Davydov, V. Y., "Phonon structure of InN grown by atomic layer epitaxy," Solid State Communications **110** (9), 491-495 (1999).
[43] Qian, Z. G., Yu, G., Shen, W. Z., Ogawa, H. and Guo, Q. X., "Growth-dependent phonon characteristics in InN thin films," Physica B: Condensed Matter **318** (2–3), 180-187 (2002).
[44] Kasic, A., Schubert, M., Saito, Y., Nanishi, Y. and Wagner, G., "Effective electron mass and phonon modes in \textit{n} -type hexagonal InN," Physical Review B **65** (11), 115206 (2002).
[45] Wu, J., Walukiewicz, W., Shan, W., Yu, K. M., Ager, J. W., Haller, E. E., Lu, H. and Schaff, W. J., "Effects of the narrow band gap on the properties of InN," Physical Review B **66** (20), 201403 (2002).
[46] Darakchieva, V., Paskov, P. P., Valcheva, E., Paskova, T., Schubert, M., Bundesmann, C., Lu, H., Schaff, W. J. and Monemar, B., "Infrared ellipsometry and Raman studies of hexagonal InN films: correlation between strain and vibrational properties," Superlattices and Microstructures **36** (4–6), 573-580 (2004).
[47] Kasic, A., Valcheva, E., Monemar, B., Lu, H. and Schaff, W. J., "InN dielectric function from the midinfrared to the ultraviolet range," Physical Review B **70** (11), 115217 (2004).
[48] Nag, B. R., "Electron mobility in indium nitride," Journal of Crystal Growth **269** (1), 35-40 (2004).
[49] Thakur, J. S., Auner, G. W., Haddad, D. B., Naik, R. and Naik, V. M., "Disorder effects on infrared reflection spectra of InN films," Journal of Applied Physics **95** (9), 4795-4801 (2004).
[50] Inushima, T., Fukui, K., Lu, H. and Schaff, W. J., "Phonon polariton of InN observed by infrared synchrotron radiation," Applied Physics Letters **92** (17), 171905 (2008).

[51] Cuscó, R., Ibáñez, J., Alarcón-Lladó, E., Artús, L., Yamaguchi, T. and Nanishi, Y., "Raman scattering study of the long-wavelength longitudinal-optical-phonon\char21{}plasmon coupled modes in high-mobility InN layers," Physical Review B **79** (15), 155210 (2009).
[52] Kim, J. G., Kamei, Y., Hasuike, N., Harima, H., Kisoda, K., Sasamoto, K. and Yamamoto, A., "Effective mass of InN estimated by Raman scattering," physica status solidi (c) **7** (7-8), 1887-1889 (2010).
[53] Thakur, J. S., Dixit, A., Danylyuk, Y. V., Sudakar, C., Naik, V. M., Schaff, W. J. and Naik, R., "Investigation of E[sub 1](LO) phonon-plasmon coupled modes and critical points in In[sub 1 - x]Ga[sub x]N thin films by optical reflectance measurements," Applied Physics Letters **96** (18), 181904 (2010).
[54] Tiras, E., Tanisli, M., Balkan, N., Ardali, S., Iliopoulos, E. and Georgakilas, A., "Determination of the carrier density dependent electron effective mass in InN using infrared and Raman spectra," physica status solidi (b) **249** (6), 1235-1240 (2012).
[55] Fu, S. P. and Chen, Y. F., "Effective mass of InN epilayers," Applied Physics Letters **85** (9), 1523-1525 (2004).
[56] Ishitani, Y., Xu, K., Terashima, W., Hashimoto, N., Yoshitani, M., Hata, T. and Yoshikawa, A., "Infrared measurements of InN films at low temperatures," physica status solidi (c) **0** (7), 2838-2841 (2003).
[57] Fukui, K., Kugumiya, Y., Nakagawa, N. and Yamamoto, A., "Infrared reflectance measurement for InN thin film characterization," physica status solidi (c) **3** (6), 1874-1878 (2006).
[58] Schley, P., Goldhahn, R., Gobsch, G., Feneberg, M., Thonke, K., Wang, X. and Yoshikawa, A., "Influence of strain on the band gap energy of wurtzite InN," physica status solidi (b) **246** (6), 1177-1180 (2009).
[59] Himmerlich, M., Knübel, A., Aidam, R., Kirste, L., Eisenhardt, A., Krischok, S., Pezoldt, J., Schley, P., Sakalauskas, E., Goldhahn, R., Félix, R., Mánuel, J. M., Morales, F. M., Carvalho, D., Ben, T., García, R. and Koblmüller, G., "N-type conductivity and properties of carbon-doped InN(0001) films grown by molecular beam epitaxy," Journal of Applied Physics **113** (3), 033501 (2013).